nature nanotechnology

Article

https://doi.org/10.1038/s41565-022-01297-9

Solving integral equations in free space with inverse-designed ultrathin optical metagratings

In the format provided by the authors and unedited

In this supplementary information file, we provide the S-matrix definitions and the ports configuration at the core of the design strategy and kernel optimization. We describe the optimization routine that results in the optimum metagrating unit cell. Next, we discuss the impact of fabrication imperfections on the performance of the proposed analog optical computing scheme and use this analysis to benchmark our experimental data giving an estimate of the solution experimentally provided by the metastructure. We add further applications of the concepts described in the main text and discuss possibilities and limitations concerning scaling up the problem dimensionality. Finally, the setup used for the optical characterization in Fig. 5 of the main text is shown and described.

Kernel design

The first step in the design is carefully defining and labeling the input/output ports. The system is addressed by six ports corresponding to six different diffraction channels at angles $\theta_0 = \sin^{-1}\left(\lambda_0/p\ n_{sup}\right)$, $\theta_T = \sin^{-1}\left(\lambda_0/p\ n_{sub}\right)$ where λ_0 is the free–space wavelength of operation, p is the grating periodicity and n_{sup}, n_{sub} are the superstrate and substrate refractive indices respectively. The plane waves probing the system via these diffraction channels are TE polarized and the linear relationship between these incident, transmitted and reflected waves defines the scattering matrix (or S-matrix) of the system. The s-parameters defining this matrix are complex numbers normalized such that $\left|\mathsf{S}_{ij}\right|^2$ is the transmittance to port i when port j is illuminated (taking into account refractive indices and angles). It is useful to write Eq. (3) of the main text in an expanded form to visualize the position of each s-parameter in the matrix and to connect it to the corresponding couple of input/output ports

$$\mathsf{S}_1 = \begin{pmatrix} \mathsf{S}_{1R} & \mathsf{S}_{1T}{}^{\intercal} \\ \mathsf{S}_{1T} & \mathsf{S}_{1R'} \end{pmatrix} = \begin{pmatrix} r_{11} & r_{12} & r_{13} & t_{14} & t_{15} & t_{16} \\ r_{21} & r_{22} & r_{23} & t_{24} & t_{25} & t_{26} \\ r_{31} & r_{32} & r_{33} & t_{34} & t_{35} & t_{36} \\ t_{41} & t_{42} & t_{43} & r_{44} & r_{45} & r_{46} \\ t_{51} & t_{52} & t_{53} & r_{54} & r_{55} & r_{56} \\ t_{61} & t_{62} & t_{63} & r_{64} & r_{65} & r_{66} \end{pmatrix} \tag{1}$$

Figure 1 shows the input/output ports configuration including the related reference planes for the metagrating, the entire metastructure and the semi-transparent mirror along with the corresponding S-matrices. As mentioned in the main text, the kernel design boils down to only the optimization of the sub-block S_{1R} as the Neumann series involves only the ports in reflection.

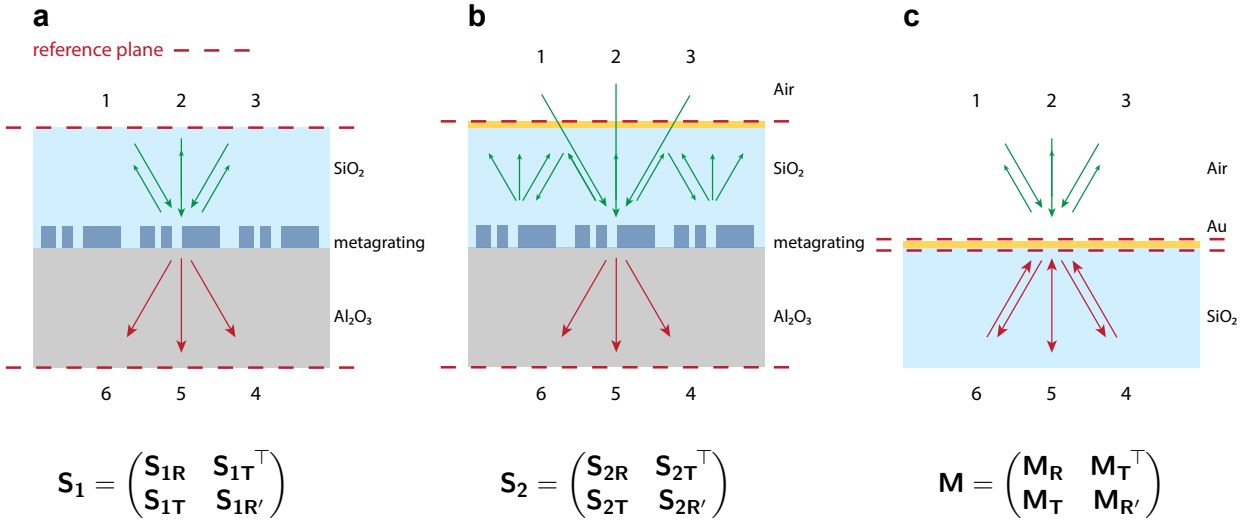

Figure 1. Schematics of the input and output ports including the related reference planes for **a** metagrating, **b** entire metastructure and **c** semi-transparent mirror. The corresponding S-matrix is underneath each panel.

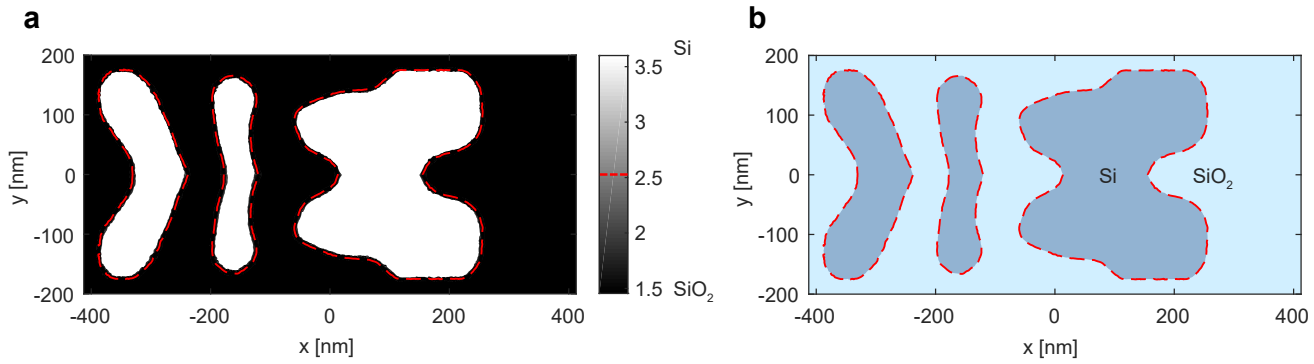

Figure 2. **a** Optimized unit cell refractive index distribution (grayscale). Black indicates the index of SiO_2 while white indicates that of Si. The colormap is continuous even if it appears binarized. The red dashed line indicated the contour used to generate the final unit cell. **b** Binarized metagrating unit-cell made of silicon (blue) and SiO_2 (light blue).

The kernels that can be mapped are limited by the fact that the final structure is passive and does not break Lorentz reciprocity. The choice of working with the reflective part of the s-matrix allows for a configuration that it is easier to fabricate experimentally but limits the generality of the kernels that can be implemented to symmetric ones. However, these concepts may be extended to more general kernels by optimizing the transmissive block of the s-matrix and with an appropriate feedback system. The energy constraint makes it impossible to map unbounded problems while kernels with eigenvalues larger the unity in amplitude shall be scaled down normalizing by their largest eigenvalue; more information on this procedure along with a detailed description of the conditions of convergence is reported in the Supplementary Information of reference[1]. Any other well behaved arbitrary symmetric kernel can be mapped onto the metagrating S-matrix with a reasonable N. In the proposed metastructure passivity is insured by Si losses and by the mirror semi-transparency.

Inverse design techniques were utilized in order to create a design which satisfied the constraints contained within S_{1R}. Specifically, the grating unit cell topology is optimized employing COMSOL Multiphysics's optimization module. The figure of merit that is minimized is the sum of the distances on the complex planes between the optimized s-parameters and the chosen kernel. Also, polarization conversion is minimized as it would open extra channels effectively changing the dimension of S_1. During the optimization, the unit cell permittivity distribution is periodically blurred to avoid small features that are hard to fabricate and a soft step function is applied to drive the optimum toward a more binary configuration. Also, the mesh size was reduced along the iterations to increase the accuracy of the simulation. Once the desired figure of merit is reached for an experimentally feasible unit cell, the permittivity distribution is fully binarized: all the domains with a refractive index below and above the threshold $(n_{Si}+n_{SiO_2})/2 \simeq 2.6$ are converted to SiO_2 and Si respectively therefore obtaining the final unit cell design. Furthermore, by changing this threshold, it is possible to generate expanded and eroded designs that are used to study the design tolerance to fabrication imperfections.

Processing time

In order to estimate the processing time we calculate the average error incurred due to truncation as a function of the number of iterations. We define the truncated Neumann series as

$$\mathsf{S}_{\text{trunc}} = \mathsf{S}_{1\mathsf{T}}\mathsf{M}_{\mathsf{T}} + \sum_{n=1}^{N} \mathsf{S}_{1\mathsf{T}} \left(\mathsf{M}_{\mathsf{R}'}\mathsf{S}_{1\mathsf{R}}\right)^n \mathsf{M}_{\mathsf{T}}. \tag{2}$$

We can then give an estimate of the total error by summing up and averaging the distance between the elements of $\mathsf{S}_{\text{trunc}}$ and those of $\mathsf{S}_{2\mathsf{T}} = \mathsf{S}_{1\mathsf{T}} \left(\mathbb{I}_3 - \mathsf{M}_{\mathsf{R}'}\mathsf{S}_{1\mathsf{R}}\right)^{-1} \mathsf{M}_{\mathsf{T}}$ on the complex plane.

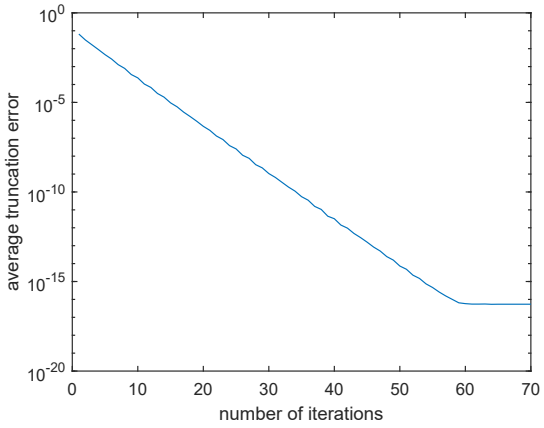

Figure 3. Average error incurred due to truncation as a function of the number of iterations (i.e. terms in the Neumann series).

Figure 3 shows this estimate as a function of the truncation order N. After 60 iterations the error becomes smaller than the standard double precision (IEEE Standard 754) used to represent floating numbers (i.e. 64 bits). The time employed by light to perform this number of interactions with the grating (2 passes per interaction) is t_{60} = 349 fs. This time is still orders of magnitude below one CPU clock period. For a better comparison, we measured the time it takes our lab server (Intel Xeon Silver 4216) to compute $\mathsf{S}_{1\mathsf{T}}\left(\mathbb{I}_3 - \mathsf{M}_{\mathsf{R}'}\mathsf{S}_{1\mathsf{R}}\right)^{-1}\mathsf{M}_{\mathsf{T}}$ and found it to be $63\mu s$. It is worth highlighting that the truncation error being smaller than double precision is only used as a threshold to estimate the processing time and does not correspond to the total error on the solution of the equation.

Design robustness and experimental solution estimate

Figure 4 shows the robustness of the metagrating based integral equation solver concept against fabrication imperfections. First, the experimental refractive indices of the annealed silica sol-gel and sputtered SiO_2, measured with ellipsometry, are included in the simulations. Next, several unit cell contours are generated from the distribution in Fig. 2a by sweeping the binarization threshold (see Fig. 4a); this type of fabrication imperfection may rise from unintended resists over- or underexposure. The transmittance corresponding to these slightly eroded and expanded unit cells is simulated and compared to the experimental transmittance data showed in Fig. 4 of the main text. Both for the bare metasurface and for the metasurface including the SiO_2 spacer, the experimental data is bounded by the transmittance of an expanded unit cell (level 2.2) and that of an eroded one (level 3.2) being remarkably close to the data of a slightly eroded unit cell (level 2.8). Nonetheless, it is crucial to evaluate the impact of the described imperfections on the performance of the integral solver. For each unit cell the S-matrix was simulated and $\mathsf{S}_{1\mathsf{R}}$ plotted in Fig. 4d-f.

The consequence of the mentioned shape distortion is a shift in the operational wavelength. In fact, the minimum distance between the prescribed S-parameters and the simulated ones (i.e. the minimum FOM) is achieved at a different wavelength, which is blue-shifted for the eroded pattern and red-shifted for the expanded counterpart. Also, the FOM value at the minimum depends on the unit cell shape and this has a direct impact on the accuracy of the solution provided by the entire metastructure including the feedback semi-transparent mirror. Figure 4 g-i shows how the solution obtained with the three different contours compares to the ideal one. The overall trend is well represented, both in real and imaginary part, even for non-ideal designs and for the different input vectors $(1,0,0)^\intercal$, $(0,1,0)^\intercal$, $(0,0,1)^\intercal$. Similar results are obtained upon including additional nonidealities such as sloped sidewalls introducing only a small shift in wavelength and a small accuracy loss.

Next, we can use this fabrication tolerances analysis to benchmark our experimental data and give an estimate

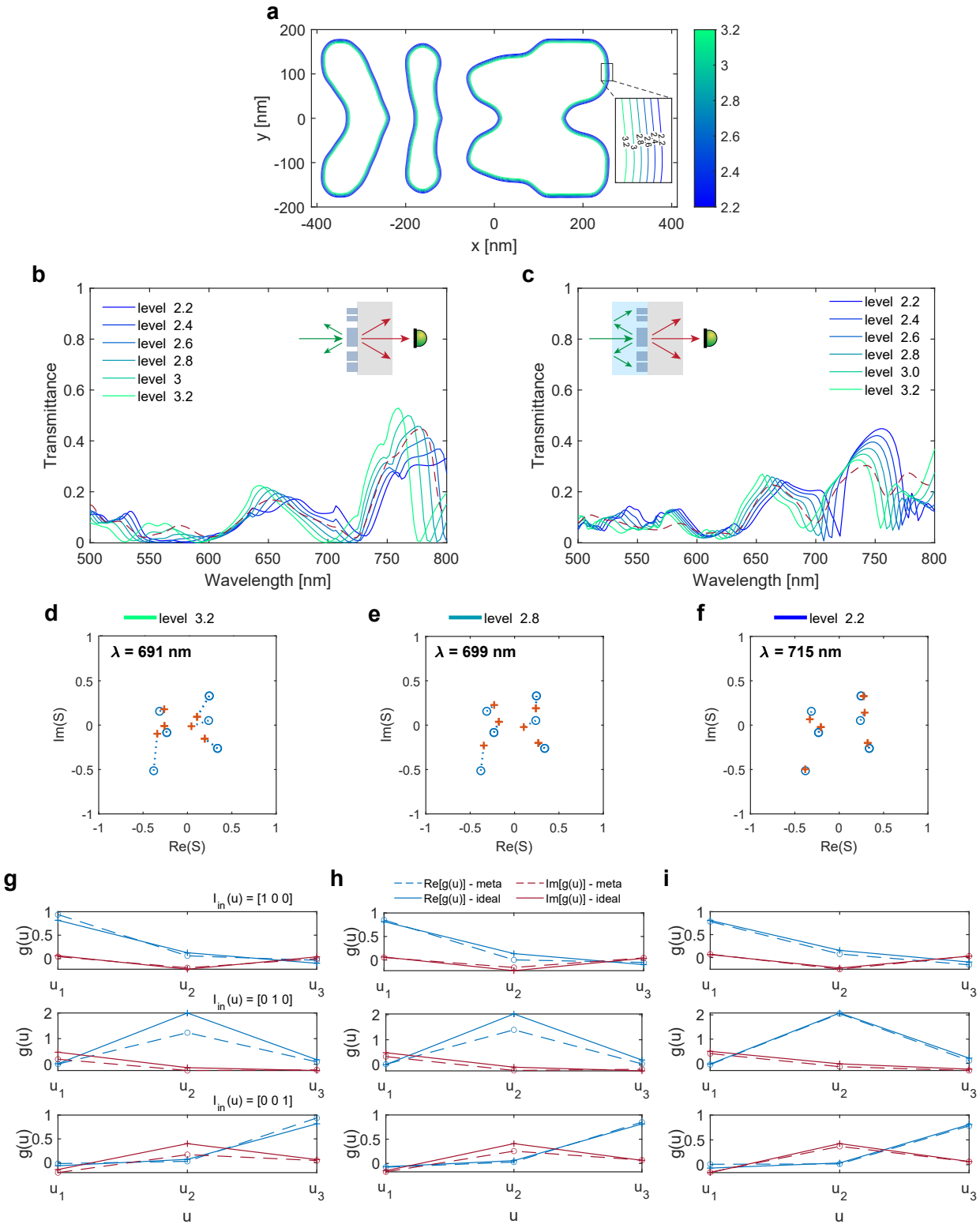

Figure 4. **a** Expanded and eroded contours generated from the optimal unit cell refractive index distribution in Fig. 2a. **b** Simulated (solid lines) transmittance spectra (0^{th} transmitted diffraction order) of the metagrating for the contours shown in a. The red dashed line is the experimental transmittance also shown in Fig. 4c of the main text. **c** Same as panel b but including the SiO_2 spacer layer. **d–f** Simulated S_{1R} s-matrix sub block for three different unit cell contours (levels 2.2, 2.8, 3.2). **g–i** Comparison between the analog solution obtained from the simulated metastructure transmission and the ideal solution for the same three contours as in d-f and for the three different orthogonal input vectors.

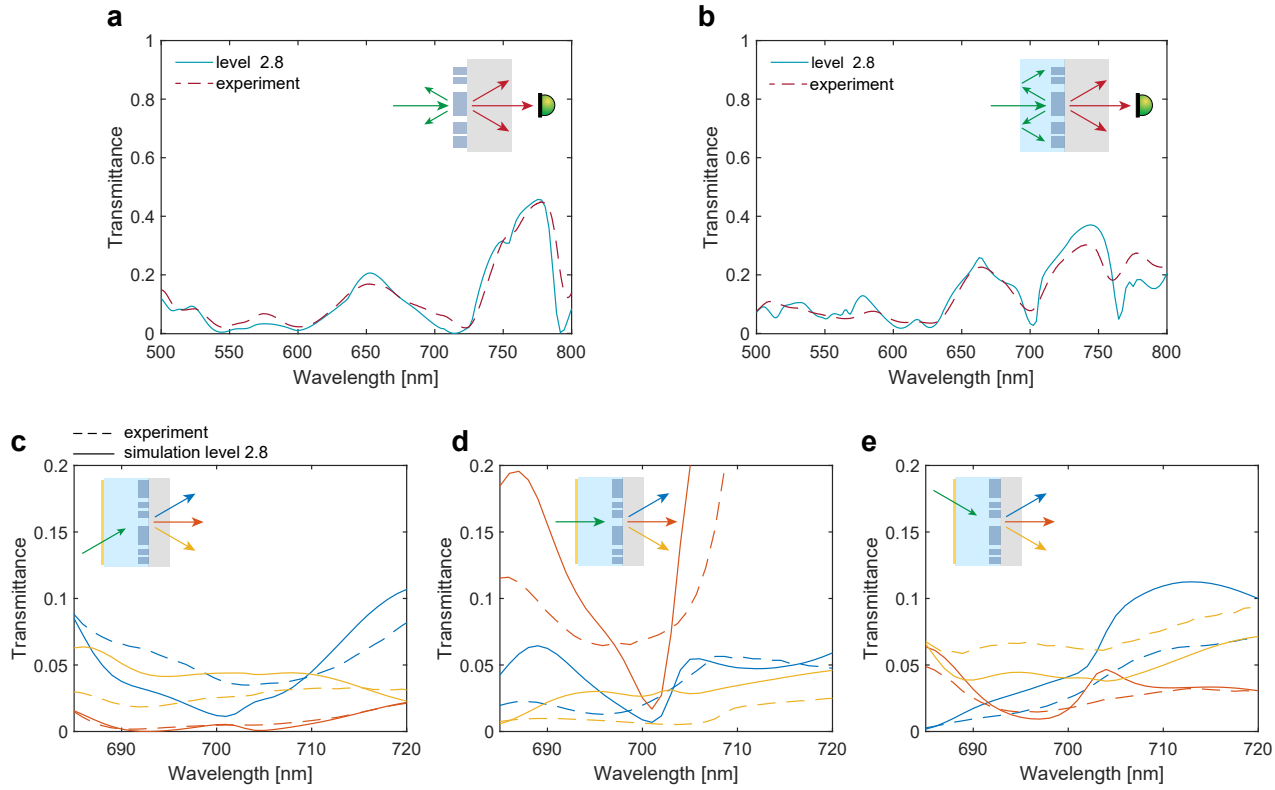

Figure 5. **a** Simulated (solid lines) transmittance spectra (0^{th} transmitted diffraction order) of the metagrating for the contour level 2.8. The red dashed line is the experimental transmittance also shown in Fig. 4c of the main text. **b** Same as panel a but including the SiO_2 spacer layer. **c–e** Experimental (dashed lines) and simulated (solid lines - contour level 2.8) transmittance spectra of the completed metastructure. Insets: schematic visualization of the metastructure indicating the exciting input port (green arrows) representing orthogonal unit vectors, and the three output ports (yellow, orange, and blue matching the corresponding spectra).

of the solution experimentally provided by the metastructure. In fact, it is possible to treat the contour level (i.e. binarization threshold) as a fitting parameter to find the closest matching simulation to the experimental data. Figure 5a-b shows the simulated 0^{th}–order transmittance spectra for a slightly eroded unit cell (level 2.8) and its experimental counterpart for the bare metagrating and including the SiO_2 spacer layer. The agreement over a broad wavelength range between simulation and experiment is very good. Figure 5c-e compares the experimental and simulated (contour level 2.8) transmittance spectra of the fully fabricated metastructure relating to each S-parameter belonging to $|S_{2T}|^2$ in a narrower spectral range around the designed wavelength of operation. Again, the experimental spectra reproduce the key features present in the simulated counterpart with rather small deviations. However, in order to validate the use of the simulation with contour level 2.8 as the estimated experimental solution it is important to assess the impact of such deviations. To do so, we use the generated expanded and eroded designs (contour levels from 2.2 to 3.2) to define a confidence region that bounds our experimental transmittance spectra.

Figure 6 shows that, even though the experimental data does not correspond perfectly to one specific simulation, at $\lambda = 699$ nm the transmittance lies in the range defined by the simulations with the only exception of the matrix element S_{61} that differs from it by less than 1%. Hence, it is possible to select the solution corresponding to contour level 2.8 attributing to it an uncertainty defined by the response of all the other contours at the same wavelength $\lambda = 699$ nm. Figure 7 shows the final estimated experimental solution equipped with the latter uncertainty region. The metasurface-based analog solution and the ideal solution show good agreement and similar trend for all the inputs, both in terms of the real and imaginary parts. Furthermore, most of the values corresponding to the ideal

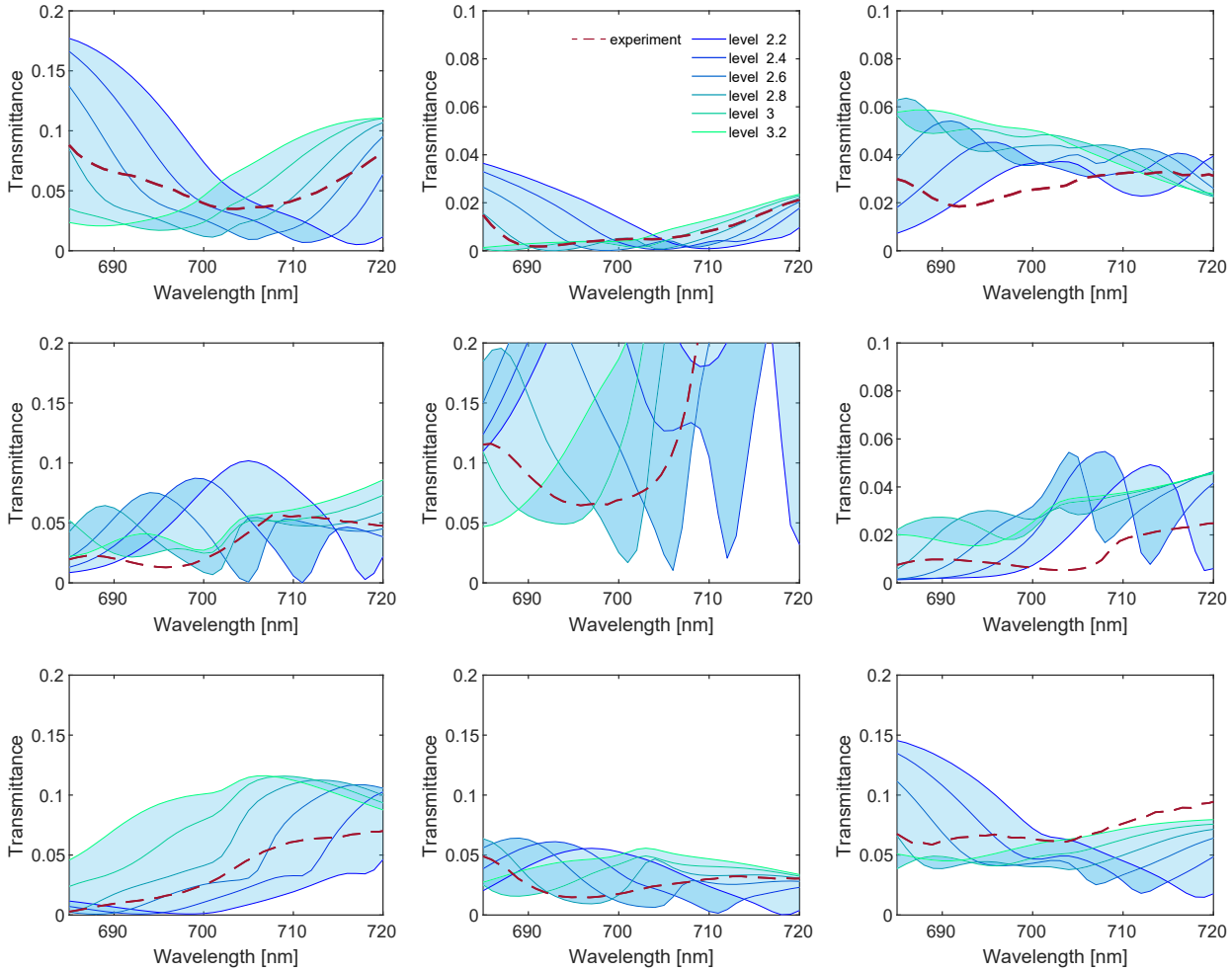

Figure 6. **a** Experimental (dashed lines) and simulated (solid lines - contour levels 2.8–3.2) transmittance spectra of the completed metastructure. Each panel corresponds to one element of the matrix $\mathsf{S}_{2\mathsf{T}}$.

solution are compatible with the estimated experimental solution (i.e. lie in its uncertainty region).

To conclude, while fabrication imperfections have certainly an impact on the overall accuracy, they do not hinder the concept of solving an integral equation with the proposed optical-analog scheme. Moreover, we showed how to retrieve via simulations the solution provided by the metastructure via measuring its response in amplitude in a broad spectral range.

Supplementary note

The same metagrating-feedback iterative approach can be applied also to Fredholm integral equations of the first kind. Indeed, by designing on purpose the kernel to be $\mathsf{K}' = \mathbb{I}_N - \mathsf{K}$ the solution provided by the metastructure would be $\mathbf{g} = \mathsf{K}^{-1}\,\mathbf{I}_{\text{in}}$ which is the solution of the Fredholm integral equation of the first kind $\mathbf{I}_{\text{in}} = \mathsf{K}\,\mathbf{g}$. Also, we envision the possibility of solving the homogeneous equation corresponding to the Fredholm integral equation of the second kind under study by exploiting, for example, spontaneous emission of active materials.

Moreover, it is possible to scale up the dimensionality of the problem, increasing the number of input/output ports by using more diffraction orders or by encoding information in the polarization state of light. Here, $N = 3$ was used as a proof of concept however a slight increase to the periodicity w (that was set subwavelength) would open 3 extra out-of-plane diffraction channels and enable a 6×6 kernel. In fact, the dimensionality of the problem scales quite quickly with the periodicity. It is worth highlighting that in the current design all the cross-polarization

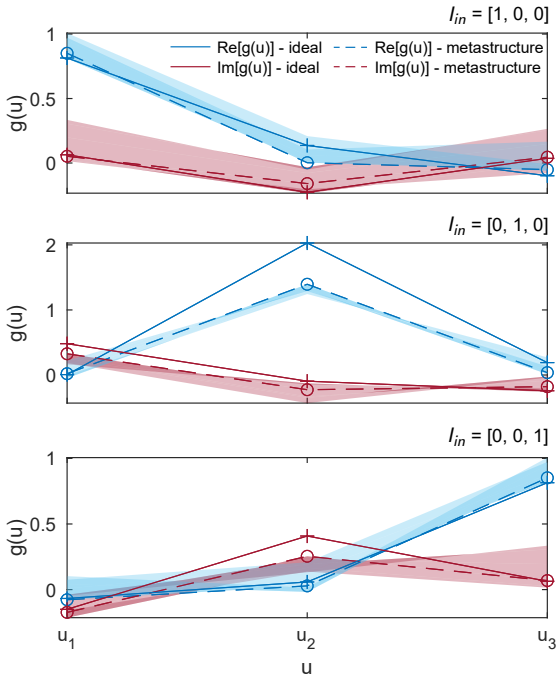

Figure 7. Estimated experimental analog solution (real and imaginary parts) of the integral equation (dashed line) compared to the ideal theoretical solution, for the three orthogonal input vectors $(1,0,0)^\intercal$, $(0,1,0)^\intercal$, $(0,0,1)^\intercal$. The wavelength of operation in this simulation is $\lambda = 699$ nm. The shaded regions indicate the uncertainty related to the solution and are generated by the response of several simulation with expanded and eroded designs.

terms are set to zero. This was done for simplicity. However, this means that our design effectively corresponds to a 6×6 matrix. For some applications, this magnitude of dimensionality is already relevant, for example, if the kernel $K(u,v)$ to be sampled does not vary quickly as a function of the variables u and v. The main challenge in scaling up the dimensionality lies in one's ability to accurately fabricate unit cells of higher resolution and smaller feature size required to sustain many optical modes and hence independently control the coupling to more diffraction orders[2,3]. Of course, a larger number of diffraction orders would imply a larger periodicity and unit cell, partially easing this burden. Also, it is possible to design similar metastructures at larger wavelengths (e.g. telecom wavelengths) while still taking advantage of e-beam lithography's resolution. In addition, thicker or even layered metagratings could further boost the available degrees of freedom required for the kernel design. The system can be illuminated with any arbitrary complex input vector, and the solution can be readily measured as output vector without having to adapt the structure. For large N, the input function could be encoded in an impinging image while the output image is analyzed in Fourier space and acquired on a CCD chip.

Methods: supplementary figure

Figure 5 in the main text shows the measured transmittance spectra of the fully fabricated metastructure relating to each S-parameter belonging to S_{2T} or, equivalently, the fraction of transmitted light going into each diffraction channel when the metastructure is illuminated through each input channel above the mirror. Specifically, each sub-panel shows the amplitudes squared of the elements belonging to each column of S_{2T}. Note that the input and output angles are changing with the wavelength of illumination according to the grating equation. In order to collect this data, the setup in in Fig. 8 was used. The illumination is provided by the same SuperK EXTREME/FIANIUM supercontinuum white-light laser that is monochromated (2 nm bandwidth) by a Laser Line Tunable Filter (LLTF) from Photon Etc. The setup consists of two concentric rotating stages. The sample is mounted on the inner rotating stage (Rot. stage 1 in Fig. 8) while an optical power meter (Power meter PM100USB with Photodiode Power Sensor

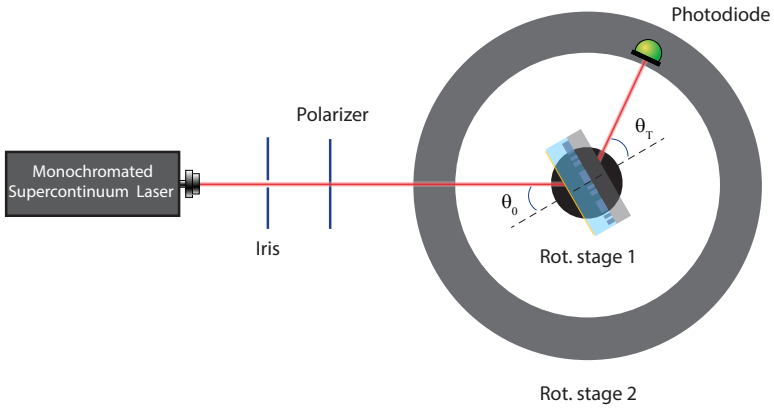

Figure 8. Schematics of the setup used to collect the data shown in Fig. 5 of the main text.

S121C from Thorlabs) is mounted on the outer rotating stage (Rot. stage 2). This configuration allows independent control of θ_0 and θ_T. Light is polarized before impinging on the sample.

References

1. Mohammadi Estakhri, N., Edwards, B. & Engheta, N. Inverse-designed metastructures that solve equations. *Science* **363**, 1333–1338, DOI: 10.1126/science.aaw2498 (2019).
2. Large-Angle, Multifunctional Metagratings Based on Freeform Multimode Geometries. *Nano Lett.* **17**, 3752–3757, DOI: 10.1021/acs.nanolett.7b01082 (2017).
3. Optical properties of deep lamellar Gratings: A coupled Bloch-mode insight. *J. Light. Technol.* **24**, 2442–2449, DOI: 10.1109/JLT.2006.874555 (2006).